The Planetary Science Journal, 2:20 (11pp), 2021 February https://doi.org/10.3847/PSJ/abc95c

Testing Short-term Variability and Sampling of Primary Volatiles in Comet 46P/Wirtanen

Younas Khan[1,10], Erika L. Gibb[1,10], Boncho P. Bonev[2,10], Nathan X. Roth[3,4,10], Mohammad Saki[1,10], Michael A. DiSanti[4,10], Neil Dello Russo[5,10], Ronald J. Vervack, Jr.[5,10], Adam J. McKay[2,4,10], Michael R. Combi[6], Yinsi Shou[6], Martin A. Cordiner[4,7], Hideyo Kawakita[8,10], Nicolas Fougere[6], and Silvia Protopapa[9]
[1] Department of Physics and Astronomy, University of Missouri-St. Louis, One University Boulevard, St. Louis, MO, USA; younas.khan@mail.umsl.edu
[2] Department of Physics American University 4400 Massachusetts Avenue NW Washington, DC 20016, USA
[3] Universities Space Research Association Columbia, MD, USA
[4] Solar System Exploration Division Code 690, NASA-Goddard Space Flight Center, Greenbelt, MD, USA
[5] Johns Hopkins Applied Physics Laboratory, Laurel, MD, USA
[6] Department of Climate and Space Sciences and Engineering, University of Michigan, Ann Arbor, MI, USA
[7] Department of Physics, Catholic University of America, Washington DC, USA
[8] Koyama Astronomical Observatory Kyoto Sangyo University Motoyama, Kamigamo, Kita-ku, Kyoto, 603-8555, Japan
[9] Southwest Research Institute, Boulder, CO, USA
Received 2020 September 30; revised 2020 November 5; accepted 2020 November 7; published 2021 February 1

Abstract

The exceptionally favorable close approach of Jupiter-family comet 46P/Wirtanen in 2018 December enabled characterization of its primary volatile composition with exceptionally high spatial resolution and sensitivities using the iSHELL spectrograph at the NASA Infrared Telescope Facility on Maunakea, HI. We sampled emissions from H_2O, HCN, C_2H_2, NH_3, C_2H_6, and CH_3OH on UT 2018 December 21 using two instrumental settings that spanned the 2.9–3.6 μm spectral region. We also obtained a sensitive 3σ upper limit for H_2CO and for the rarely studied molecule HC_3N. We report rotational temperatures, production rates, and mixing ratios (relative to H_2O as well as to C_2H_6). We place our results in context by comparing them with other comets observed at near-IR wavelengths. We also compare our results with those obtained using the NIRSPEC-2 spectrograph on Keck II on UT December 17 and 18 and with results obtained from iSHELL on other dates during the same apparition. Within 1–2σ uncertainty, production rates obtained for all molecules in this work were consistent with those obtained using NIRSPEC-2 except H_2O, indicating low-level variability on a timescale of days. Mixing ratios with respect to H_2O in 46P/Wirtanen were consistent with corresponding values from NIRSPEC-2 within the uncertainty with the exception of CH_3OH, which yielded a higher ratio on December 21. Our measurements afforded a high temporal resolution that spanned ~2/3 of the rotational period of 46P/Wirtanen, enabling us to test short-term variability in the production rates of H_2O and HCN due to rotational effects. Both H_2O and HCN production rates showed similar temporal variability, resulting in nearly constant HCN/H_2O.

Unified Astronomy Thesaurus concepts: Comet volatiles (2162); Near infrared astronomy (1093); Molecular spectroscopy (2095); Comets (280); High resolution spectroscopy (2096); Comae (271)

1. Introduction

Comets are relatively unprocessed remnants of the early solar system. As some of the first objects to have accreted in the cold regions (>5 au) of the solar nebula, comets may retain the compositional record of icy materials present in the solar nebula. Processes that can affect the properties of cometary nuclei generally alter a very thin layer near the surface, which is thought to be lost during a typical perihelion passage (Stern 2003; Gronoff et al. 2020), preserving the primitive nature of comets. Furthermore, because comets lack a known mechanism for internal heating owing to their small sizes, their present-day composition may reflect the chemistry and prevailing conditions in the early solar system where they formed ~4.5 billion years ago (Bockelée-Morvan et al. 2004; Mumma & Charnley 2011).

Initially, it was widely accepted that Oort Cloud comets (OCCs) formed at a heliocentric distance (R_h) of ~5–30 au, whereas Jupiter-family comets (JFCs) formed even farther out in the early solar nebula. However, the presence of crystalline silicates in comets from both dynamical classes, such as C/2001 Q4 (NEAT; Wooden et al. 2004), 1P/Halley (Bregman et al. 1987), 9P/Tempel 1 (Harker et al. 2005), and 81P/Wild 2 (Zolensky et al. 2006), and improved dynamical models (Levison & Duncan 1997; Gomes et al. 2005; Morbidelli et al. 2005; Levison et al. 2011; Nesvorný et al. 2017) suggest that comets may have formed in large but spatially overlapping regions in the solar nebula (A'Hearn et al. 2012). Considering these distinct versus overlapping formation region scenarios, an important goal in cometary science is to ascertain whether systematic differences exist between the chemical compositions of these two dynamical classes of comets. If comets were formed in overlapping regions, their present-day composition may reflect the composition in those regions provided that evolutionary effects do not dominate. On the other hand, if post-formation thermal processing effects dominate in comets, these effects will be more pronounced in JFCs (owing to their frequent and repeated passages close to the Sun) as compared to OCCs (Combi et al. 2019).

[10] Visiting Astronomer at the Infrared Telescope Facility, which is operated by the University of Hawai'i under contract NNH14CK55B with the National Aeronautics and Space Administration.

Near-IR spectroscopy is a powerful tool to characterize the primary volatiles (i.e., gases subliming directly from the nucleus and thus indicative of its native composition) in comets by sampling the rovibrational transitions of a suite of molecules between ∼2.9–5 μm. To date, roughly 40 comets have had their volatile composition characterized in the near-IR, but only ∼15 of those have been JFCs. Emerging trends suggest that on average JFCs are depleted in some parent volatiles (especially in hypervolatiles) as compared to OCCs (Dello Russo et al. 2016). In contrast, more than 200 comets have been sampled at optical wavelengths, (A'Hearn et al. 1995; Fink 2009; Cochran et al. 2012; Schleicher & Bair 2014) where nearly one-third exhibit depletion in carbon-chain species. Of these, about half are JFCs whereas only 10% are OCCs, suggesting that the compositional differences between the two dynamical classes may be natal rather than due to post-formation processing (Schleicher 2007; Dello Russo et al. 2009; Fink 2009).

The highly favorable apparition of 46P/Wirtanen (hereafter 46P) in 2018 was the focus of a worldwide observing campaign (http://wirtanen.astro.umd.edu). 46P reached its perihelion on UT 2018 December 12, with a heliocentric distance (R_h) of ∼1.05 au. Shortly after its perihelion, it reached a minimum geocentric distance of 0.077 au (∼30 lunar distances) and a visual magnitude of ∼3, resulting in exceptional observing circumstances for a JFC. It remained within a distance of 0.1 au from Earth for ∼20 consecutive days, allowing for detailed observations by both professional and amateur astronomers.

46P was the original target of the Rosetta spacecraft mission; however, 67P/Churyumov–Gerasimenko was selected for the mission due to a delay in launch. We emphasize that knowledge of the overall activity and composition is often an important parameter in assessing the suitability of a comet as a mission target. It is also useful in placing mission data in context with the much larger database of remote-sensing observations of comets. The historic 2018 apparition of 46P thus provided a timely opportunity for sampling the primary volatile composition of a JFC that remains a favorable candidate for a future mission.

The importance of 46P as a JFC, coupled with the exceptional and rare observing conditions during its 2018 apparition, lends great significance to these observations, as well as to the scientific knowledge that will be extracted from them. Moreover, distinguishing between natal versus post-formation processing effects in OCCs and JFCs requires comparison of a sufficiently large sample of comets from each dynamical class. Sampling of the chemical composition of 46P using near-IR spectroscopy is a useful addition to the overall comet inventory as well as to the generally underrepresented JFCs.

An increasing number of comets measured to date have displayed variability in their coma composition within an apparition as well as across perihelion passages. This variability has been attributed to numerous effects, including seasonal effects on the nucleus, diurnal illumination effects, and chemically heterogeneous nuclei (Feaga et al. 2014; Hässig et al. 2015; Luspay-Kuti et al. 2015; McKay et al. 2015; Bockelée-Morvan et al. 2016; Fink et al. 2016; Combi et al. 2020b). Surface regions of some comets were observed to have been covered by thermally processed fall-back material. For example, the north hemisphere of 67P/Churyumov–Gerasimenko (Keller et al. 2017) and the waist of 103P/Hartley 2 (A'Hearn et al. 2011; Kelley et al. 2013) are covered by processed material. However, the coma activity was dominated by the fresh material emitted by the southern hemisphere of 67P/Churyumov–Gerasimenko and ends of the small lobe of 103P/Hartley 2. This mass transfer on comet nuclei due to fall-back material may affect their surface evolution and is an example of post-formation processing.

Remote-sensing observations do not resolve the nucleus, and time-resolved compositional measurements through a complete nucleus rotation are lacking at near-IR wavelengths. Jehin et al. (2018) reported a ∼9 hr rotational period for 46P using a CN lightcurve measured from photometry obtained at the TRAPPIST telescopes on UT 2018 December 9–10. The relatively short rotational period of 46P provided us with an opportunity to sample ∼2/3 of its period during a single observing night on UT 2018 December 21, and to test for rotational variability in HCN and H_2O on a timescale of a few hours.

In this work, we report production rates and mixing ratios (i.e., abundance ratios in percent) of H_2O, HCN, CH_3OH, C_2H_6, C_2H_2, and NH_3 with respect to H_2O and C_2H_6 and report stringent 3σ upper limits for H_2CO and HC_3N. We also discuss possible variability in the production rates of H_2O and HCN in comet 46P post-perihelion. In Section 2, we review our observations and data reduction. In Section 3, we present our results. In Section 4, we discuss our results and place them into context with comets observed to date.

2. Observations and Data Reduction

iSHELL at the NASA Infrared Telescope Facility (IRTF) became available for cometary observations in 2016 (Rayner et al. 2012, 2016). This instrument is capable of both high-resolution long-slit spectroscopy and imaging in the 1.1–5.3 μm range, with a spectral resolving power ($\lambda/\Delta\lambda$) of up to 7.5×10^4 using its narrowest slit (0.″375). Extra slit widths are available for minimizing slit losses and accurate flux calibration. Owing to its cross-dispersed capability, iSHELL can measure a signal in more than ten consecutive echelle orders simultaneously, whereas its daytime observing capability allows for observations of objects best observed during daylight hours, namely comets close to the Sun. These features make iSHELL unique among contemporary spectrographs operating in the near-IR wavelength regime.

We observed 46P post-perihelion on UT 2018 December 21 at R_h ∼1.06 au and geocentric distance (Δ) ∼0.082 au (see Table 1 for observing details). We used the iSHELL Lp1 and a custom L setting (hereafter L-custom) to sample emissions from the primary volatiles H_2O, HCN, CH_3OH, C_2H_6, C_2H_2, NH_3, H_2CO, and HC_3N. Flux calibration was achieved using a bright nearby IR flux standard star (BS8781) using the 4″ wide slit. We acquired comet data with the 0.″75 (6 pixel) wide slit using an ABBA nod sequence, with the A and B beams placed symmetrically about the midpoint along the 15″ long slit and separated by half its length. To cancel continuum emissions from the thermal background, instrumental biases, and sky emission (lines and continuum), the spectra were combined as A–B–B+A. The dark subtracted flats were applied to the data, which were subsequently cleaned of cosmic-ray hits and hot pixels. We alternated between two slit orientations while using the L-Custom setting: one along the Sun–comet line (position angle, PA 134°) and the other orthogonal to the Sun–comet line (PA 44°), with each slit orientation sampling a unique projection of the coma into the sky plane. Our observations spanned ∼2/3 of a complete rotation for 46P. In this way we obtained a total of four separate observations, with two sets

Table 1
Observing Log for 46P/Wirtanen on UT 2018 December 21

iSHELL Setting	Slit PA (deg)	Wavelength Range (cm^{-1})	Time (UT)	R_h(au)	Δ (au)	Δ-dot (km s^{-1})	T_{int} (minute)
Lp1	134	2750–3060	5:45–6:02	1.061	0.082 5	3.379	16
L-Custom	134	3210–3580	6:10–7:29	1.061	0.082 5	3.379	72
L-Custom	44	〃	7:43–8:52	1.061	0.082 6	3.561	64
L-Custom	134	〃	8:57–10:07	1.061	0.082 7	3.713	64
L-Custom	44	〃	10:21–11:55	1.061	0.082 8	3.867	84

Note. Slit PA, R_h, Δ, Δ-dot, and T_{int} are the slit position angle, heliocentric distance, geocentric distance, geocentric velocity, and total on-source integration time, respectively.

each corresponding to the mutually perpendicular slit orientations (see Table 1).

The data-reduction procedures have been rigorously tested and are well-documented in the literature (see Bonev 2005; DiSanti et al. 2006, 2014; Villanueva et al. 2009; Radeva et al. 2010). For their applications to unique aspects of iSHELL spectra, see Section 3.2 of DiSanti et al. (2017).

Contributions from continuum and gaseous emissions in our spectra were determined as previously described by DiSanti et al. (2016). We illustrate the procedure in Figure 1, which shows a sample spectrum of H_2O fluorescent emissions in order 179 of the third PA set of the L-Custom setting spanning ∼3437.8–3465.8 cm^{-1}. We used the Planetary Spectrum Generator (https://psg.gsfc.nasa.gov/; Villanueva et al. 2018) to generate telluric transmittance models, to perform wavelength calibration of the spectra, and to determine column burdens of the absorbing molecules in the terrestrial atmosphere. The fully resolved transmittance function was convolved to the resolving power ($\sim 4.5 \times 10^4$) of the instrument and scaled to the continuum level of the comet. The telluric model was then subtracted from the observed spectrum to isolate cometary emission lines. Intensities of these emission lines were compared to fluorescent emission models after correcting each modeled line intensity for the monochromatic atmospheric transmittance at its Doppler-shifted wavelength based on the geocentric velocity (∼3.4–3.9 km s^{-1}) of the comet at the time of the observation.

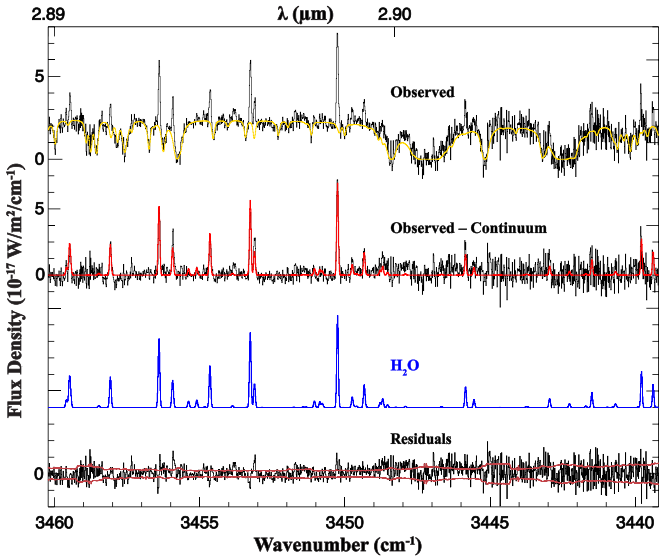

Figure 1. Extracted spectrum showing clear detection of H_2O fluorescent emission lines. In the upper portion, the telluric absorption model (yellow; convolved to the instrumental resolution) has been overplotted on the observed cometary spectrum. Directly below, the H_2O fluorescent model (red) is overplotted on the cometary emission spectrum (after subtracting the telluric absorption model). The fluorescent model for H_2O is also shown separately in blue. The residual spectrum (after subtracting the telluric model and the fluorescent model) is shown at the bottom of the figure along with the 1σ uncertainty envelope.

3. Results

3.1. Spatial Profiles

A comparison between spatial profiles of co-measured coma volatiles can indicate whether these species sublimated directly from the comet nucleus, from one or more extended outgassing sources within the coma, or a combination of both. In general, ices sublimating directly from the nucleus exhibit a spatial profile that peaks in intensity at or near the nucleus and then falls off as r^{-1}, where r is the projected nucleocentric distance. On the other hand, spatial profiles of molecules produced by photolysis or extended sources in the coma fall off more slowly with a flatter distribution. Figure 2 shows spatial profiles of co-measured HCN and H_2O along with the dust continuum in each PA set of the L-Custom setting. In each of these sets, the gas profiles track each other somewhat closely whereas the dust profile is narrower. The gas profiles are also asymmetric and are extended in the projected anti-sunward direction. These asymmetries are more pronounced in the first two PA sets (Figures 2(A) and (B)). Figure 3 shows spatial profiles of co-measured CH_3OH and C_2H_6 overplotted with the dust profile. The relatively noisy CH_3OH spatial profile is broader than both the co-measured C_2H_6 as well as dust profile, whereas both of the gas profiles are broader than the dust profile. An anti-sunward extension in gas profiles is also evident. We note that spatial profiles of all of these gases appear to be consistent with their growth factors (GFs; defined as Q/Q_{NC} where Q and Q_{NC} are the global and nucleus-centered production rates, respectively); i.e., H_2O and HCN GFs are relatively similar whereas the CH_3OH GF is significantly larger than that of C_2H_6 (see Table 2).

3.2. Molecular Fluorescence Analysis

The *g-factors* used in this work were generated with quantum mechanical models developed for H_2O (Villanueva et al. 2012b), C_2H_6 (Villanueva et al. 2011b), CH_3OH (Villanueva et al. 2012a; DiSanti et al. 2013), H_2CO (DiSanti et al. 2006), C_2H_2 (Villanueva et al. 2011a), NH_3 (Villanueva et al. 2013), and HCN (Lippi et al. 2013). HC_3N is a simple

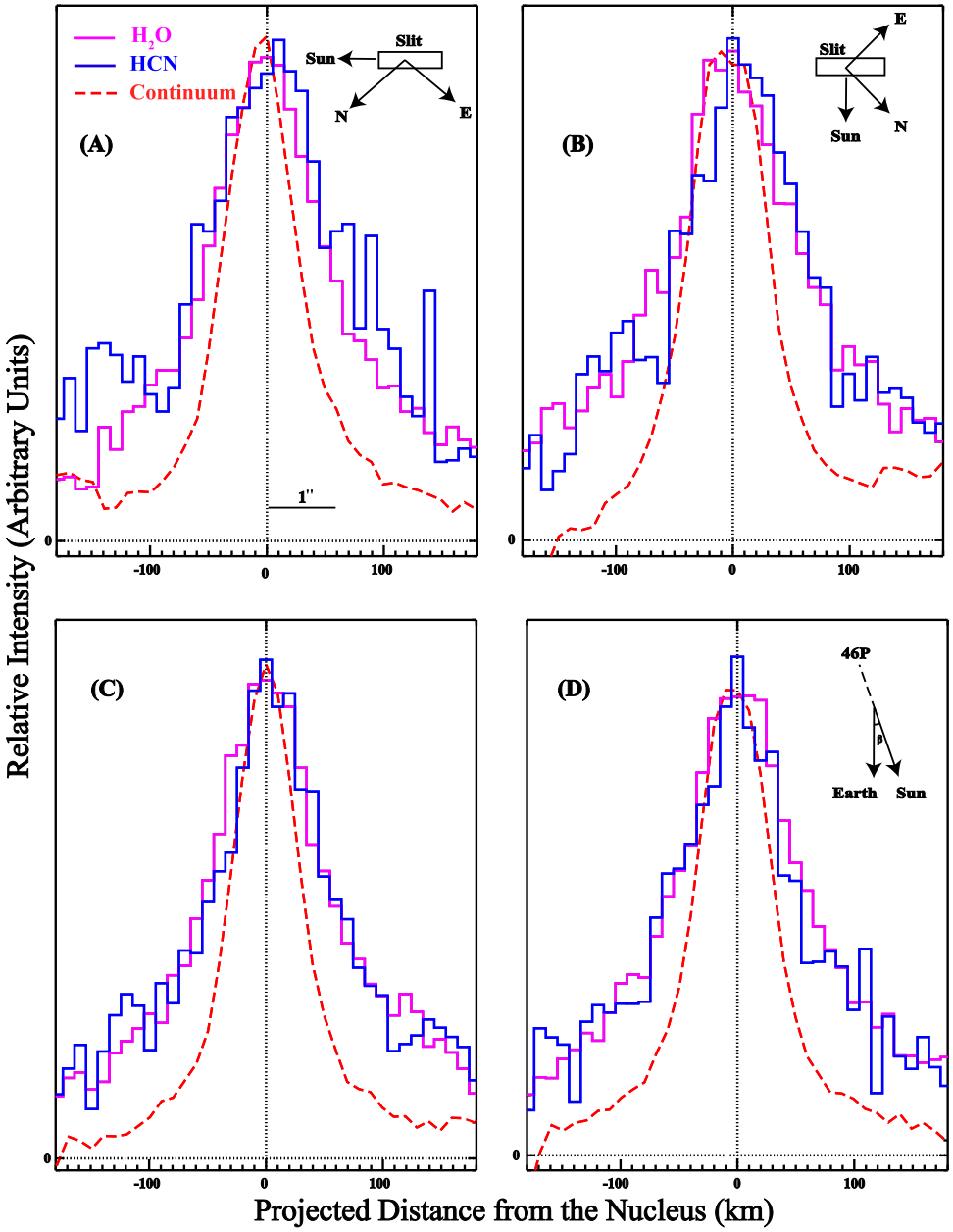

Figure 2. Spatial profiles of co-measured H_2O (pink solid line), HCN (blue solid line), and the continuum from dust (red dashed line) on UT 2018 December 21. Panels (A)–(D) correspond to PA 134°, 44°, 134°, and 44°, respectively. The horizontal bar indicating 1″ corresponds to a projected distance of ∼60 km at the geocentric distance of 46P. The Sun–comet–Earth angle (phase angle, β) of 19° is also shown.

linear molecule, and its *g-factors* were obtained using a rotational constant of 0.151 74 cm^{-1} (Creswell et al. 1977). To fit fluorescent emissions from all molecules simultaneously in each echelle order, a Levenberg–Marquardt nonlinear minimization technique (Villanueva et al. 2008) was used. This technique allows for results with high precision even in spectrally crowded regions having many lines within a single resolution element of the instrument. Production rates for each targeted primary volatile were then determined from the corresponding synthetic model at a well-constrained rotational temperature (T_{rot}).

3.3. Determination of Rotational Temperature (T_{rot})

Calculating a robust rotational temperature (T_{rot}) is crucial for an accurate calculation of molecular production rates and, hence, mixing ratios. We determined T_{rot} using correlation and excitation analyses (Bonev 2005; Bonev et al. 2008; DiSanti et al. 2006). In general, a well-constrained T_{rot} can be derived for molecules with strong lines that span a broad range of excitation energies. For this work, these conditions were satisfied by combining lines from different orders to obtain T_{rot} for H_2O in each PA set of the L-Custom setting (see Table 2). These values were similar to the H_2O T_{rot} obtained on UT December 14 (84 ± 3) (Saki et al. 2020), UT December 17 (89 ± 2) and UT December 18 (87 ± 1) with NIRSPEC-2 (Bonev et al. 2021), and (94 ± 5) on December 18 with iSHELL (Roth et al. 2021). We also obtained a relatively well-constrained T_{rot} for HCN in each PA set by combining lines from different orders. In general, rotational temperatures calculated for different molecules using IR observations are consistent, and small variations in T_{rot} result

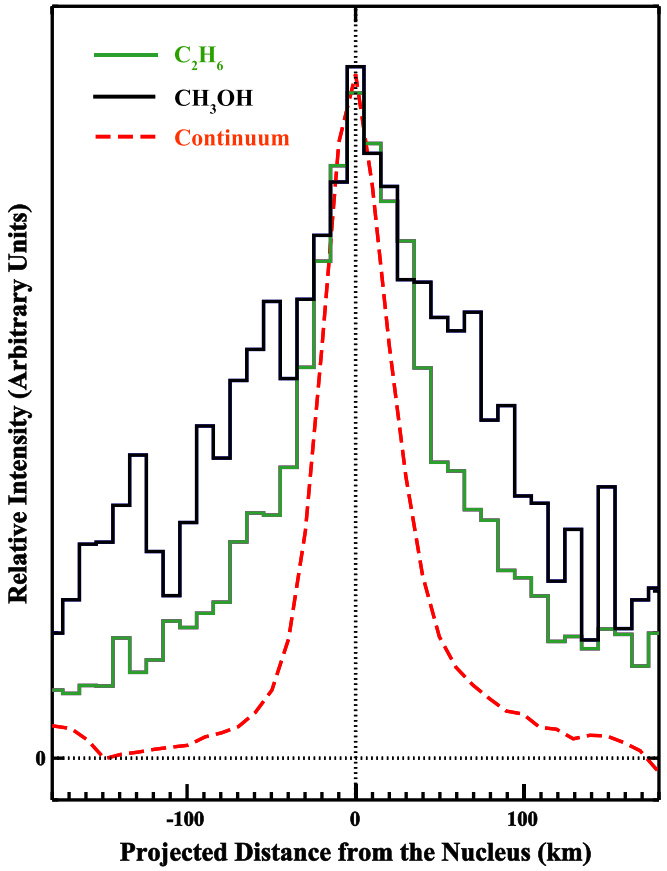

Figure 3. Spatial profiles of co-measured C_2H_6 (green solid line), CH_3OH (black solid line), and dust (red dashed line) obtained using the Lp1 setting with PA of 134°.

in only minor differences in production rates (Gibb et al. 2012). For this reason, we assumed a T_{rot} of 80 K (consistent with the H_2O and HCN T_{rot} across all PA sets) for molecules where a rotational temperature could not be derived (i.e., C_2H_6, CH_3OH, H_2CO, C_2H_2, NH_3, and HC_3N).

3.4. Determination of Molecular Production Rates

Nucleus-centered production rates (Q_{NC}) and global production rates (Qs) were determined using the well-established *Q*-curve method described in Xie & Mumma (1996), Dello Russo et al. (1998), DiSanti et al. (2001, 2016), Bonev (2005), Bonev et al. (2006, 2017), Villanueva et al. (2011a), and Gibb et al. (2012). This method provides a GF that corrects for atmospheric seeing, which suppresses the signal along lines of sight passing close to the nucleus due to the use of a narrow slit, as well as potential perpendicular drift of the comet during an exposure sequence. We assumed a canonical spherically symmetric outflow velocity ($v_{gas} = 800\, R_h^{-0.5}$ m s^{-1}) in determining production rates. This velocity is based on velocity-resolved observations of several moderately bright comets at radio wavelengths (Biver et al. 2006; Cordiner et al. 2014; also see Bonev 2005 supporting this assumption). We note that our assumed outflow velocity (∼780 m s^{-1}) is in good agreement with the sunward hemisphere and with mean expansion speeds (∼800 and ∼700 m s^{-1}, respectively) measured through velocity-resolved Atacama Large Millimeter/submillimeter Array (M. A. Cordiner et al. 2021, in preparation) and the Institut de Radioastronomie Millimétrique (N. Biver 2020, private communication) observations. Reasonably contemporaneous to our observations, Wang et al. (2020) and Coulson et al. (2020) reported outflow velocities of 500 and 600 m s^{-1}, respectively. Assuming these lower outflow velocities will decrease the overall production rates by ∼20%, but does not significantly change the mixing ratios. We obtained GFs for H_2O and HCN in each PA set of the L-Custom setting and used them to calculate co-measured H_2O and HCN production rates in each PA set. We could not obtain well-constrained GFs for the weaker species C_2H_2, NH_3, and HC_3N; therefore, we used a GF of 2.2 (consistent with the H_2O GFs across all PA sets) for these species. Similarly, we obtained GFs for CH_3OH and C_2H_6 and used the CH_3OH GF to get an upper limit on co-measured H_2CO. GFs, Qs, and mixing ratios with respect to H_2O (and to C_2H_6) corresponding to all primary volatiles targeted in this work are listed in Table 2. We note that Qs for all molecules were obtained by adding lines from multiple orders. For deriving HCN mixing ratios in each PA set, we used the co-measured H_2O production rate. For mixing ratios of all other molecules, we used the H_2O production rate obtained by adding lines from multiple orders within a PA set and then coadding all of those L-Custom sets.

3.5. Potential Variability in the Production Rates of H_2O and HCN

Figure 4 shows variation in the production rates of H_2O and HCN during observations spanning ∼6 hr. We obtained four sets using the L-Custom setting by varying the slit PA by 90° after each individual set (see Section 2). Both species are color coded and the corresponding error bars are also shown, along with range of UT time corresponding to each set. For clarity, HCN production rates have been vertically offset. H_2O and HCN production rates obtained in each PA set of the L-Custom setting are shown in Table 2.

3.6. Coma Volatile Composition of 46P

Figures 5(A)–(C) shows spectra of HCN, C_2H_2, NH_3, CH_3OH, and C_2H_6. Fully leveraging the large spectral grasp of iSHELL, we combined lines for weaker species that were sampled in multiple orders simultaneously in each individual slit orientation set, followed by coadding all of the L-custom sets. In this way, we were able to increase the signal-to-noise and detect the generally weaker species C_2H_2 and NH_3, which are offset vertically in the figure.

Being the dominant volatile in most comet nuclei, H_2O is used as a baseline for calculating mixing ratios of primary volatiles in comets (the exception being C/2016 R2, Pan-STARRS; McKay et al. 2019). In addition to its dominance of the volatile content of most comets, strong lines of H_2O (or its proxy, OH^*, prompt emission; Bonev et al. 2006) are available throughout the 2–5 μm region and can be sampled simultaneously with the lines of trace species, minimizing the effects of potential production rate variability when calculating mixing ratios.

Alternate compositional baselines utilizing other species satisfying these conditions can provide complementary insights into the volatile content of comets. In addition to H_2O, we therefore calculated mixing ratios of primary volatiles with respect to C_2H_6. These measurements will help motivate the development of taxonomies based on alternative compositional baselines in future work. C_2H_6 generally tends to exhibit a

Table 2
Primary Volatile Composition of Comet 46P/Wirtanen on UT 2018 December 21

Molecule	Growth Factor[a]	T_{rot}[b]	Q[c] (10^{25} mol s^{-1})	Mixing Ratio[d]	
				(H_2O = 100)	(C_2H_6 = 1)
			Lp1		
C_2H_6	1.64 ± 0.04	(80)	4.12 ± 0.5	0.71 ± 0.09	1.00
CH_3OH	2.40 ± 0.09	(80)	24.9 ± 1.6	4.26 ± 0.34	6.03 ± 0.75
H_2CO	(2.40)	(80)	<0.78	<0.13	<0.19
			L-Custom (PA 134°)		
H_2O	2.21 ± 0.10	81 ± 1	579 ± 28	100	140 ± 17
HCN	2.38 ± 0.07	79^{+6}_{-5}	1.19 ± 0.07	0.21 ± 0.01	0.29 ± 0.04
			L-Custom (PA 44°)		
H_2O	2.26 ± 0.05	81 ± 1	659 ± 20	100	160 ± 18
HCN	2.36 ± 0.12	78 ± 4	1.71 ± 0.1	0.26 ± 0.02	0.42 ± 0.05
			L-Custom (PA 134°)		
H_2O	2.15 ± 0.07	82 ± 3	590 ± 27	100	143 ± 17
HCN	2.00 ± 0.06	75^{+7}_{-6}	1.28 ± 0.07	0.22 ± 0.01	0.31 ± 0.04
			L-Custom (PA 44°)		
H_2O	2.22 ± 0.05	87 ± 1	577 ± 17	100	140 ± 16
HCN	2.18 ± 0.08	89^{+7}_{-6}	1.17 ± 0.07	0.20 ± 0.01	0.28 ± 0.04
C_2H_2[c]	(2.20)	(80)	0.46 ± 0.04	0.08 ± 0.01	0.11 ± 0.02
NH_3[c]	(2.20)	(80)	2.91 ± 0.35	0.50 ± 0.06	0.71 ± 0.12
HC_3N[c]	(2.20)	(80)	<0.04	<0.007	<0.01

Notes.
[a] GF = Q/Q_{NC}. Values in parentheses are assumed.
[b] Rotational temperature. Values in parentheses are assumed and are chosen to be consistent with H_2O and HCN T_{rot} obtained from different PA sets of the L-Custom setting.
[c] Global production rate. For C_2H_2, NH_3, and HC_3N, we added lines from all PA sets to get production rates. For all other molecules, Qs were obtained by adding lines from multiple orders within a setting. Uncertainty in production rates includes line-by-line deviation between observed and modeled intensities and photon noise (see Dello Russo et al. 2004; Bonev 2005; Bonev et al. 2007). They also include uncertainties in GFs and flux calibration, which were determined by calculating the standard deviation of flux calibration from eight exposures.
[d] Mixing ratio of global production rates with respect to H_2O (in percent) and C_2H_6. For deriving the HCN mixing ratio in each PA set, we used the corresponding H_2O production rate. For all other molecules, we used an H_2O production rate of 584 × 10^{25} mol s^{-1} obtained by adding lines from all PA sets of the L-Custom setting.

distinct outgassing behavior compared to H_2O, its sublimation temperature is among the lowest, and it is relatively easy to detect in the near-IR wavelength range. These characteristics make C_2H_6 one of the suitable molecules that can be used as an alternative compositional baseline (for a comprehensive discussion on the value of alternative baseline compositional studies and the case for C_2H_6, see Sections 4.4 and 5.4.2 of Bonev et al. (2021)).

4. Discussion

4.1. Testing Possible Variability in Production Rates

Ground-based remote-sensing observations do not resolve the nucleus of a comet (and thus do not permit identifying individual active regions on the surface), and the limited observation time available generally inhibits sampling of the full surface of a comet during a rotation cycle. There are only a few comets for which the nucleus has been resolved—those visited by spacecraft. As a comet rotates on its axis, different regions of its surface are exposed to solar irradiation, resulting in the activation of distinct sublimation regions on the nucleus. If the nucleus is heterogeneous, this may lead to variability in the composition of coma primary volatiles (e.g., in comet 67P/Churyumov–Gerasimenko; Hässig et al. 2015; Luspay-Kuti et al. 2015).

During our observations, the nucleus of 46P rotated by ∼225°, which is about two-thirds of its rotational period. During this time, the sub-solar point changed its position on the surface by ∼195° (Knight et al. 2020), and the illumination switched from one hemisphere to the other, emphasizing the significance of our time series of measurements. Production rates of H_2O and HCN during this period showed a similar trend across the four PA sets: the second PA set showed relatively higher production rates for both species indicating

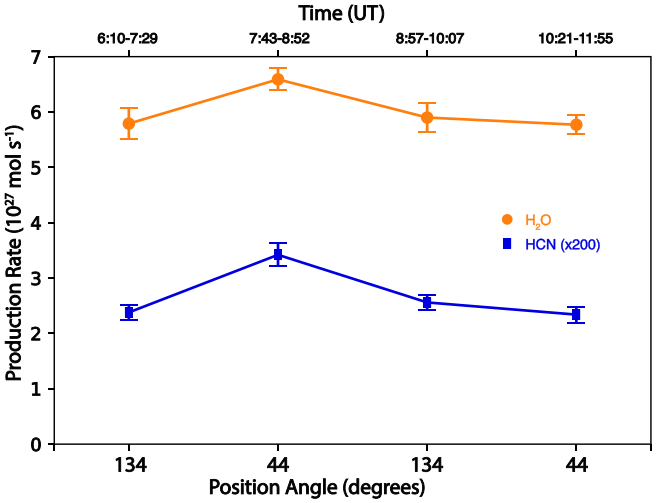

Figure 4. Production rates of H_2O and HCN (corresponding to different slit position angles used) on UT 2018 December 21, from 6:10 to 11:55. The presented time series covers ~2/3 of the rotational period, during which illuminated regions of the comet changed significantly.

low-level variability, whereas the production rates corresponding to all other PA sets were consistent with each other within the uncertainty. The mixing ratio of HCN with respect to H_2O, however, remained nearly constant across all of the PA sets. (see Table 2 and Figure 4). We note that the spatial profiles (Figure 2) are similar in each PA set, and the enhancement in production rates is only in one, suggesting that the differences are due to time variability rather than due to nonuniform spatial distributions, for example. Wang et al. (2020) reported moderate time variability in the HCN production rate in 46P on December 14 and 15 using radio observations of the HCN ($J = 1$–0) transition. They also reported asymmetric HCN outgassing, although they found that the asymmetric enhancement was in the sunward direction. Due to time constraints, we were not able to sample a full rotation period (~9 hr) of 46P; therefore, searches for variability on timescales greater than or equal to a single rotation period must be addressed in future perihelion passages of 46P.

4.2. *Composition of 46P in the Context of JFCs, OCCs, and the Comet Population Measured at Near-IR Wavelengths*

The classification of comets based on their volatile composition (both primary and product species) is an important but complex task in cometary science. Over the past few decades, extensive work at optical wavelengths has resulted in a taxonomic classification of comets based on abundances of their product species. According to this scheme, comets can be classified as "typical" or "carbon-chain depleted" (A'Hearn et al. 1995; Cochran et al. 2012 and references therein); however, tying product species abundances directly to those of their parents is a complex endeavor given their potentially complicated lineage (i.e., multiple potential volatile parents as well as dust for a given product species). More recent work based on the composition of product species in comets (Schleicher & Bair 2014; Cochran et al. 2015) suggested that there can be as many as seven taxonomic groups owing to the complex chemical diversity in comets. Observations of comets using radio techniques have shown no evidence of clear taxonomic groupings (Crovisier et al. 2009;

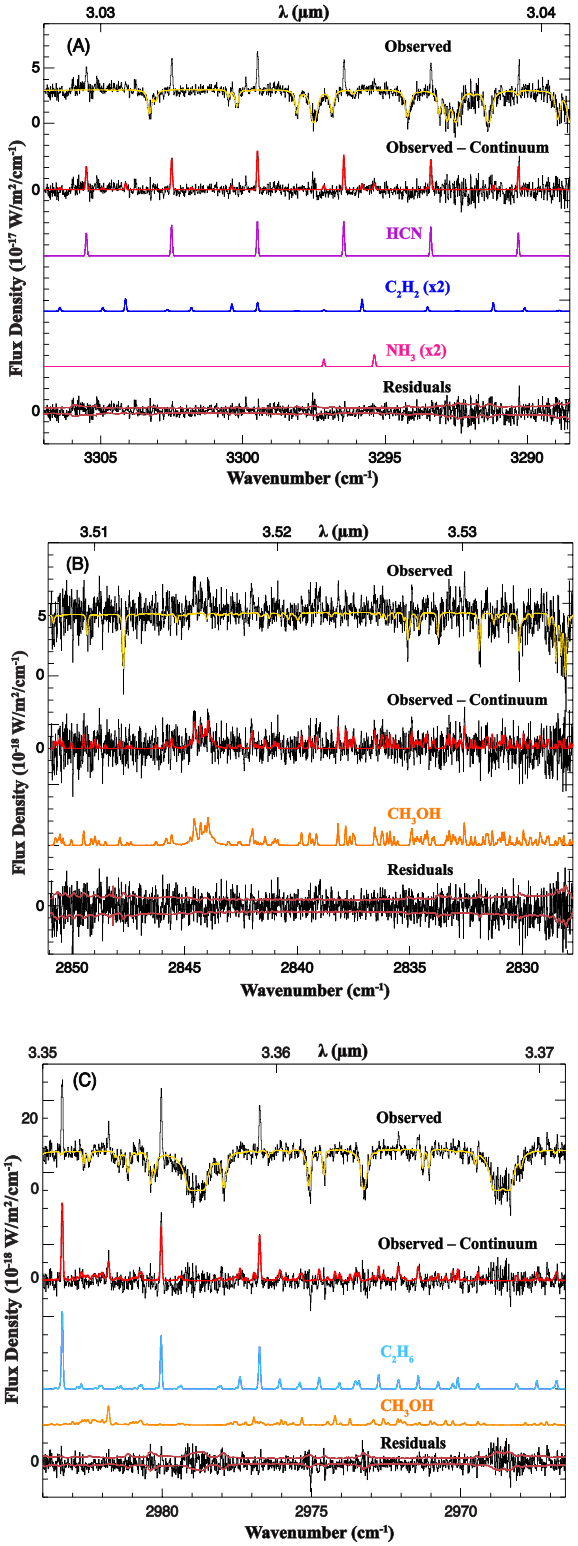

Figure 5. Extracted spectra showing clear detections of HCN, C_2H_2, NH_3 (A), CH_3OH (B), and C_2H_6 (C). In each of these panels, the upper portion shows the telluric absorption model (yellow; convolved to the instrumental resolution) overplotted on the observed cometary spectrum. Directly below, the total of individual fluorescent models (red) is overplotted on the cometary emission spectrum (after subtracting the telluric absorption model). Individual fluorescent models for each molecule (color coded by species) are also shown. The residual spectrum (after subtracting the telluric model and all fluorescent models) is shown at the bottom along with the 1σ uncertainty envelope. Models for species with weaker emission lines (C_2H_2 and NH_3) have been vertically offset for clarity.

Table 3
Mixing Ratios (Percent, with Respect to H_2O) of Primary Volatiles in 46P on UT 2018 December 21 Compared with Other Comets Observed at Near-IR Wavelengths

Molecule	Value in 46P[a]	Mean Value among JFCs[b]	Mean Value among OCCs[b]	Mean Value among Comet Population[b]
HCN	0.23 ± 0.02	0.17 ± 0.03	0.22 ± 0.03	0.21 ± 0.02
C_2H_2	0.08 ± 0.01	0.07 ± 0.02	0.16 ± 0.03	0.13 ± 0.02
NH_3	0.50 ± 0.06	0.59 ± 0.11	0.91 ± 0.30	0.80 ± 0.20
C_2H_6	0.71 ± 0.09	0.34 ± 0.07	0.63 ± 0.10	0.55 ± 0.08
CH_3OH	4.26 ± 0.34	1.73 ± 0.33	2.21 ± 0.24	2.06 ± 0.20
H_2CO	<0.13	0.26 ± 0.10	0.33 ± 0.08	0.31 ± 0.06

Notes.
[a] This work. Production rates corresponding to these values were calculated by combining lines from multiple orders and different PA sets (where applicable). The H_2O production rate used to derive these mixing ratios was obtained by combining H_2O lines from all PA sets of the L-Custom setting.
[b] Values from Dello Russo et al. (2016) calculated from 30 comets measured at near-IR wavelengths between 1997 and 2013.

Mumma & Charnley 2011 and references therein). Measurements obtained at near-IR wavelengths have resulted in a continually evolving compositional taxonomy based on primary volatiles (Mumma & Charnley 2011; Dello Russo et al. 2016). Table 3 shows the primary volatile mixing ratios of 46P on UT 2018 December 21, along with mean mixing ratios for each species among JFCs, OCCs, and the overall comet population measured at near-IR wavelengths (Dello Russo et al. 2016).

This comparison provides the following insights into the primary volatile composition of 46P in the context of dynamical classes of comets and the overall comet population:

1. Within the uncertainty, mixing ratios of HCN ($0.23 \pm 0.02\%$) and NH_3 ($0.50 \pm 0.06\%$) were consistent with their respective mean values among JFCs and OCCs.
2. The mixing ratio of C_2H_2 ($0.08 \pm 0.01\%$) was consistent with the mean value among JFCs, but depleted compared to the mean value among OCCs.
3. CH_3OH ($4.26 \pm 0.34\%$) was enriched compared to the mean abundance among JFCs and OCCs, whereas C_2H_6 ($0.71 \pm 0.09\%$) was enriched compared to the mean abundance among JFCs and consistent with the mean value among OCCs. Our measurement of CH_3OH represents one of the highest values reported in comets sampled at near-IR wavelengths to date. Comets 8P/Tuttle, C/2007 N3 (Lulin), and 2P/Encke (Bonev et al. 2008; Gibb et al. 2012; Radeva et al. 2013) showed similarly overabundant CH_3OH compared to other species. Very high abundances of CH_3OH were reported in comets 252P/LINEAR (5.56 ± 0.66%, 4.62 ± 0.48% and 4.61 ± 0.68%; Paganini et al. 2019) and 45P/Honda-Mrkos-Pajdušáková (4.60 ± 0.76% and 4.41 ± 0.77%; Dello Russo et al. 2020). Bonev et al. (2021) also reported a high mixing ratio for CH_3OH ($3.03 \pm 0.23\%$) in 46P on December 18, and suggested the possibility of an extended coma outgassing source, which is consistent with the broader spatial profile and higher GF (Figure 3, Table 2). Roth et al. (2021) also reported an enriched value of the CH_3OH mixing ratio ($2.8 \pm 0.3\%$) in 46P on December 18. Based on observations from different dates in 2019 January, McKay et al. (2021) reported an average CH_3OH mixing ratio of 2.99 ± 0.23.
4. The 3σ upper limit for H_2CO (<0.13%) suggests that its value in 46P was depleted compared with the mean values among JFCs and OCCs.
5. Compared to the mean values among the overall comet population, 46P showed enrichment in the mixing ratios of CH_3OH and depletion in C_2H_2 and H_2CO (based on the 3σ upper limit), whereas C_2H_6, HCN, and NH_3 were consistent within the uncertainty with the mean value. We note that the CH_3OH/H_2CO ratio of >33 obtained for 46P is among the highest in comets (Dello Russo et al. 2016).

This comparison suggests that 46P is not adequately described as being enriched, depleted, or average in its volatile content, reinforcing the need for a greater sampling of comets in order to develop a more complete taxonomy of comets. Abundances from the 2018 apparition of 46P are an important addition to the ever-evolving repository of comets sampled at near-IR wavelengths and to the continually evolving compositional taxonomy based on these measurements.

4.3. Sensitive Upper Limit for Cyanoacetylene (HC_3N)

Obtaining a stringent upper limit for molecules such as HC_3N is challenging because of its low abundance in comets, the presence of emission lines from many other species that can potentially cause blending, and atmospheric extinction of some lines. The continuous spectral grasp of iSHELL in the L-Custom setting allows for the simultaneous sampling of many lines of HC_3N. Combining multiple orders (spanning a frequency range of ~3316–3338 cm^{-1}) and all L-Custom observations on that night (a total of 4.715 hr of on-source integration time), coupled with the improved sensitivity of iSHELL, enabled us to derive a sensitive 3σ upper limit of HC_3N/H_2O of <0.007%. Obtaining a sensitive upper limit for an underrepresented molecule such as HC_3N in a JFC (which are generally fainter and less productive than their Oort cloud counterparts) is important for discerning the lineage of the CN radical in comets. In some comets, the production rates, scale lengths, and spatial distributions of HCN and CN are not consistent (Fray et al. 2005, and references therein), implying that CN might be produced as a result of HC_3N photolysis (Bockelée-Morvan & Crovisier 1985; Krasnopolsky et al. 1991). Similar 3σ upper limits (of the order of 10^{-3}) for HC_3N were reported by Bockelée-Morvan et al. (1987) and Swade et al. (1987) in comet P/Halley observed at radio wavelengths. Crovisier et al. (1993) reported a 3σ upper limit of <0.000 19% in radio observations of comet Levy 1990 XX.

HC_3N was first identified with radio observations of comet C/1995 O1 (Hale–Bopp; Bockelée-Morvan et al. 2000) with an abundance ratio (relative to H_2O) of 0.02%. HC_3N has since been detected in multiple comets at millimeter/submillimeter wavelengths through its pure rotational transitions, with abundances ranging from 0.002% to 0.068% (Bockelée-Morvan & Biver 2017). At near-IR wavelengths, HC_3N has been sampled in comets that include C/2009 P1 (Garradd; Villanueva et al. 2012c) with a 3σ upper limit of <0.03% and comet 103P/Hartley 2 (Dello Russo et al. 2011) with a 3σ upper limit of <0.024%. Our 3σ upper limit (<0.007%) is

Table 4
H_2O Global Production Rates in 46P in 2018 December

UT Date	H_2O Production Rate (10^{25} mol s^{-1})	Instrument
Dec 14[a]	595 ± 23	iSHELL
Dec 17[b]	749 ± 34	NIRSPEC-2
Dec 18[b]	903 ± 30	NIRSPEC-2
Dec 18[c]	825 ± 60	iSHELL
Dec 19[a]	604 ± 30	iSHELL
Dec 21[d]	579 ± 28	iSHELL
	659 ± 20	
	590 ± 27	
	577 ± 17	

Notes.
[a] Saki et al. (2020).
[b] Bonev et al. (2021).
[c] Roth et al. (2021).
[d] This work.

lower than these values, and it represents the most stringent measure of HC_3N at near-IR wavelengths to date. E. Jehin (2020, private communication) reported a Q(CN) of $(1.27 \pm 0.032) \times 10^{25}$ mol s^{-1} on UT 2018 December 16 and $(1.14 \pm 0.021) \times 10^{25}$ mol s^{-1} on December 23 in 46P using the robotic TRAPPIST-South and -North telescopes narrowband photometry. These values are relatively close to our HCN Qs in all PA sets (except for the second PA set, which resulted in a higher number), suggesting that HCN might be the predominant precursor of CN in 46P.

4.4. Comparison with iSHELL and NIRSPEC-2 Observations during the Same Perihelion Passage

Table 4 summarizes H_2O production rates in 46P on different post-perihelion dates in 2018 December. These results suggest that H_2O production rates obtained from iSHELL across other post-perihelion dates are consistent with our December 21 results, whereas those measured with NIRSPEC-2 on December 17 and 18 (Bonev et al. 2021) and with iSHELL on December 18 (Roth et al. 2021) are higher, despite only a marginal change in the geocentric and heliocentric distances of 46P between December 17 and 21 (R_h varied from 1.057 to 1.061 au between these dates; Δ varied from 0.078 to 0.082 au). This might be an indication of variability in H_2O production rates on a timescale of days (addressing possible variability in 46P during its 2018 apparition is the subject of future work). Using measurements from SOHO/SWAN, Combi et al. (2020a) reported that the overall H_2O production rate in 46P decreased significantly throughout its 1997, 2002, 2008, and 2018 apparitions along with a large steepening of the change in H_2O production rate with R_h. While these measurements do not cover the dates listed in Table 4, the H_2O production rate measured on December 22.976 ($\sim 1.6 \times 10^{28}$ mol s^{-1}) was significantly higher than our December 21 values of $\sim 6 \times 10^{27}$ mol s^{-1} with the caveat that the SOHO/SWAN measurements may be more sensitive to an extended source of water in the coma than our near-IR measurements. With the exception of H_2O, the production rates of all molecules we measured agree within 1–2σ uncertainty with values obtained from NIRSPEC-2 on UT December 17 and 18, whereas the mixing ratios we obtained agree within 1σ with values from NIRSPEC-2 with the exception that our CH_3OH mixing ratio is higher.

5. Summary and Future Outlook

We utilized the exceptional observing conditions offered by 46P/Wirtanen's historical 2018 apparition to characterize its primary volatile content and to determine the spatial associations of species in the coma. Through our measurements we obtained the following results:

(1) We obtained mixing ratios with respect to H_2O (and C_2H_6) of the primary volatiles H_2O, HCN, C_2H_2, NH_3, C_2H_6, and CH_3OH on UT 2018 December 21 using the iSHELL spectrograph at the NASA IRTF. We obtained stringent 3σ upper limits for H_2CO and also HC_3N, a molecule that has been rarely studied in comets to date.
(2) We placed the chemical composition of 46P/Wirtanen in the context of comets observed at near-IR wavelengths and found that the comet does not follow the simple three-tiered taxonomic scheme, i.e., it is not systematically enriched, depleted, or averaged in the mixing ratios of its volatiles.
(3) We were able to extract spatial profiles for co-measured HCN and H_2O in multiple, independent slit orientations of the L-Custom setting. We also obtained spatial profiles for co-measured CH_3OH and C_2H_6. Both gases exhibited broader profiles as compared to the profile from dust, whereas the CH_3OH profile was broader as compared to co-measured C_2H_6. Spatial profiles of all of the gases were asymmetric and extended in the projected anti-sunward direction.
(4) We compared production rates of HCN and H_2O obtained from mutually perpendicular slit orientations to search for potential short-term variability and found that both of these species follow a similar trend and exhibit a low-level, short-term variability.
(5) Our H_2O production rates generally agreed with those obtained on other dates post-perihelion except for measurements with iSHELL on December 18 and those obtained with NIRSPEC-2 on December 17 and 18, which yielded higher Q(H_2O), suggesting variability in the H_2O production rate over a time span of a few days.

Additional observations obtained using iSHELL and NIRSPEC during the exceptional 2018 apparition of 46P will enable future work testing for long-term variability in the comet, thus addressing the "snapshot" bias associated with cometary observations taken over a limited range of dates and/or heliocentric distances. Comparisons between dates pre-perihelion, near-perihelion, and post-perihelion will test for potential seasonal effects in 46P (e.g., Hässig et al. 2015; McKay et al. 2015; Roth et al. 2018). Observations taken with sufficient geocentric velocity will enable the study of hypervolatiles CO and CH_4 by shifting their lines away from their telluric counterparts, increasing the sample size of these underrepresented molecules in studies of JFCs (e.g., DiSanti et al. 2017; McKay et al. 2021).

Data for this study were obtained at the NASA Infrared Telescope Facility (IRTF), operated by the University of Hawai'i under contract NNH14CK55B with the National

Aeronautics and Space Administration (NASA). We are most fortunate to have had the opportunity to conduct observations from Maunakea, and we recognize and acknowledge the very significant cultural role and reverence that the summit of Maunakea has always had within the indigenous Hawaiian community. We acknowledge the commitment of NASA-IRTF to comet 46P/Wirtanen's observing campaign in its 2018 historical apparition. This study was generously funded by the NASA Planetary Astronomy/Solar System Observations (NNX12AG24G, 15-SSO15_2-0028, 18-SSO18_2-0040, and 80NSSC17K0705), the Solar System Workings Programs (NNX17AC86G and 80NSSC20K0651 [MRC, YS]), the NASA Astrobiology Institute (13-13NAI7_2_0032), the NASA Emerging Worlds Program (80NSSC20K0341), the National Science Foundation (AST-1616306, AST-1615441, AST-2009398, and AST-2009910), and NASA Headquarters under the NASA Earth and Space Science Fellowship Program (grant NNX16AP49H). We acknowledge and thank the entire staff at IRTF for their support during our observations. N.X.R. acknowledges support by the NASA Postdoctoral Program at the NASA Goddard Space Flight Center, administered by Universities Space Research Association under contract with NASA.

ORCID iDs

Younas Khan https://orcid.org/0000-0003-4773-2674
Erika L. Gibb https://orcid.org/0000-0003-0142-5265
Boncho P. Bonev https://orcid.org/0000-0002-6391-4817
Nathan X. Roth https://orcid.org/0000-0002-6006-9574
Mohammad Saki https://orcid.org/0000-0003-2277-6232
Michael A. DiSanti https://orcid.org/0000-0001-8843-7511
Neil Dello Russo https://orcid.org/0000-0002-8379-7304
Ronald J. Vervack, Jr. https://orcid.org/0000-0002-8227-9564
Adam J. McKay https://orcid.org/0000-0002-0622-2400
Michael R. Combi https://orcid.org/0000-0002-9805-0078
Martin A. Cordiner https://orcid.org/0000-0001-8233-2436
Nicolas Fougere https://orcid.org/0000-0001-9626-004X
Silvia Protopapa https://orcid.org/0000-0001-8541-8550

References

A'Hearn, M. F., Belton, M. J. S., Delamere, W. A., et al. 2011, Sci, 332, 1396
A'Hearn, M. F., Feaga, L. M., Keller, H. U., et al. 2012, ApJ, 758, 29
A'Hearn, M. F., Millis, R. L., Schleicher, D. G., Osip, D. J., & Birch, P. V. 1995, Icar, 118, 223
Biver, N., Bockelée-Morvan, D., Crovisier, J., et al. 2006, A&A, 449, 1255
Bockelée-Morvan, D., & Biver, N. 2017, RSPTA, 375, 20160252
Bockelée-Morvan, D., & Crovisier, J. 1985, A&A, 151, 90
Bockelée-Morvan, D., Crovisier, J., Despois, D., et al. 1987, A&A, 180, 253
Bockelée-Morvan, D., Crovisier, J., Erard, S., et al. 2016, MNRAS, 462, S170
Bockelée-Morvan, D., Crovisier, J., Mumma, M. J., & Weaver, H. A. 2004, in Comets II, ed. M. C. Festou, H. U. Keller, & H. A. Weaver (Tucson, AZ: Univ. Arizona Press), 391
Bockelée-Morvan, D., Lis, D. C., Wink, J. E., et al. 2000, A&A, 353, 1101
Bonev, B. P. 2005, PhD thesis, Univ. Toledo, http://astrobiology.gsfc.nasa.gov/Bonev_thesis.pdf
Bonev, B. P., Dello Russo, N., DiSanti, M. A., et al. 2021, PSJ, in press
Bonev, B. P., Mumma, M. J., DiSanti, M. A., et al. 2006, ApJ, 653, 774
Bonev, B. P., Mumma, M. J., Radeva, Y. L., et al. 2008, ApJL, 680, L61
Bonev, B. P., Mumma, M. J., Villanueva, G. L., et al. 2007, ApJ, 661, L97
Bonev, B. P., Villanueva, G. L., DiSanti, M. A., et al. 2017, AJ, 153, 241
Bregman, J. D., Witteborn, F. C., Allamandola, L. J., et al. 1987, A&A, 187, 616
Cochran, A. L., Barker, E. S., & Gray, C. L. 2012, Icar, 218, 144
Cochran, A. L., Levasseur-Regourd, A.-C., Cordiner, M. A., et al. 2015, SSRv, 197, 9
Combi, M. R., Mäkinen, T., Bertaux, J.-L., et al. 2020a, PSJ, 1, 72
Combi, M. R., Mäkinen, T. T., Bertaux, J.-L., Quémerais, E., & Ferron, S. 2019, Icar, 317, 610
Combi, M. R., Shou, Y., Fougere, N., et al. 2020b, Icar, 335, 113421
Cordiner, M. A., Remijan, A. J., Boissier, J., et al. 2014, ApJL, 792, L2
Coulson, I. M., Liu, F.-C., Cordiner, M. A., et al. 2020, AJ, 160, 182
Creswell, R. A., Winnewisser, G., & Gerry, M. C. L. 1977, JMoSp, 65, 420
Crovisier, J., Biver, N., Bockelée-Morvan, D., et al. 2009, EM&P, 105, 267
Crovisier, J., Bockelée-Morvan, D., Colom, P., Despois, D., & Paubert, G. 1993, A&A, 269, 527
Dello Russo, N., DiSanti, M. A., Magee-Sauer, K., et al. 2004, Icar, 168, 186
Dello Russo, N., DiSanti, M. A., Mumma, M. J., Magee-Sauer, K., & Rettig, T. W. 1998, Icar, 135, 377
Dello Russo, N., Kawakita, H., & Bonev, B. P. 2020, Icar, 335, 113411
Dello Russo, N., Kawakita, H., Vervack, R. J., Jr., & Weaver, H. A. 2016, Icar, 278, 301
Dello Russo, N., Vervack, R. J., Jr., Lisse, C. M., et al. 2011, ApJL, 734, L8
Dello Russo, N., Vervack, R. J., Jr., Weaver, H. A., et al. 2009, ApJ, 703, 187
DiSanti, M. A., Bonev, B. P., Dello Russo, N., et al. 2017, AJ, 154, 246
DiSanti, M. A., Bonev, B. P., Gibb, E. L., et al. 2016, ApJ, 820, 34
DiSanti, M. A., Bonev, B. P., Magee-Sauer, K., et al. 2006, ApJ, 650, 470
DiSanti, M. A., Bonev, B. P., Villanueva, G. L., & Mumma, M. J. 2013, ApJ, 763, 1
DiSanti, M. A., Mumma, M. J., Dello Russo, N., & Magee-Sauer, K. 2001, Icar, 153, 361
DiSanti, M. A., Villanueva, G. L., Paganini, L., et al. 2014, Icar, 228, 167
Feaga, L. M., A'Hearn, M. F., Farnham, T. L., et al. 2014, AJ, 147, 24
Fink, U. 2009, Icar, 201, 311
Fink, U., Doose, L., Rinaldi, G., et al. 2016, Icar, 277, 78
Fray, N., Bénilan, Y., Cottin, H., Gazeau, M.-C., & Crovisier, J. 2005, P&SS, 53, 1243
Gibb, E. L., Bonev, B. P., Villanueva, G. L., et al. 2012, ApJ, 750, 102
Gomes, R., Levison, H. F., Tsiganis, K., & Morbidelli, A. 2005, Natur, 435, 466
Gronoff, G., Maggiolo, R., Cessateur, G., et al. 2020, ApJ, 890, 89
Harker, D. E., Woodward, C. E., & Wooden, D. H. 2005, Sci, 310, 278
Hässig, M., Altwegg, K., Balsiger, H., et al. 2015, Sci, 347, aaa0276
Jehin, E., Moulane, Y., Manfroid, J., & Pozuelos, F. 2018, CBET, 4585, 1
Keller, H. U., Mottola, S., Hviid, S. F., et al. 2017, MNRAS, 469, S357
Kelley, M. S., Lindler, D. J., Bodewits, D., et al. 2013, Icar, 222, 634
Knight, M. M., Schleicher, D. G., & Farnham, T. L. 2020, PSJ, in press
Krasnopolsky, V. A., Tkachuk, A. Y., & Korablev, O. I. 1991, A&A, 245, 662
Levison, H. F., & Duncan, M. J. 1997, Icar, 127, 13
Levison, H. F., Morbidelli, A., Tsiganis, K., Nesvorný, D., & Gomes, R. 2011, AJ, 142, 152
Lippi, M., Villanueva, G. L., DiSanti, M. A., et al. 2013, A&A, 551, A51
Luspay-Kuti, A., Hässig, M., Fuselier, S. A., et al. 2015, A&A, 583, A4
McKay, A. J., Cochran, A. L., DiSanti, M. A., et al. 2015, Icar, 250, 504
McKay, A. J., DiSanti, M. A., Cochran, A. L., et al. 2021, PSJ, in press
McKay, A. J., DiSanti, M. A., Kelly, M. S. P., et al. 2019, AJ, 158, 128
Morbidelli, A., Levison, H. F., Tsiganis, K., & Gomes, R. 2005, Natur, 435, 462
Mumma, M. J., & Charnley, S. B. 2011, ARA&A, 49, 471
Nesvorný, D., Vokrouhlický, Dones, L., et al. 2017, ApJ, 845, 27
Paganini, L., Camarca, M. N., Mumma, M. J., et al. 2019, AJ, 158, 98
Radeva, Y., Mumma, M. J., Villanueva, G. L., et al. 2013, Icar, 223, 298
Radeva, Y. L., Mumma, M. J., Bonev, B. P., et al. 2010, Icar, 206, 764
Rayner, J., Bond, T., Bonnet, M., et al. 2012, Proc. SPIE, 8446, 84462C
Rayner, J., Tokunaga, A., Jaffe, D., et al. 2016, Proc. SPIE, 9908, 990884
Roth, N. X., Boney, B. P., & DiSanti, M. A. 2021, PSJ, in press
Roth, N. X., Gibb, E. L., Bonev, B. P., et al. 2018, AJ, 156, 251
Saki, M., Gibb, E., Bonev, B., et al. 2020, AJ, 160, 184
Schleicher, D. G. 2007, Icar, 190, 406
Schleicher, D. G., & Bair, A. 2014, in Proc. Asteroids Comets Meteors Conf., ed. K. Muinonen (Helsinki: Univ. Helsinki), 475
Stern, S. A. 2003, Natur, 424, 639
Swade, D. A., Schloerb, F. P., Irvine, W. M., & Kinzel, W. M. 1987, in Cometary Radio Astronomy; Proc. of the NRAO Workshop, ed. W. M. Irvine, F. P. Schloerb, & L. E. Tacconi-Garman (Green Bank, WV: NRAO), 79
Villanueva, G. L., DiSanti, M. A., Mumma, M. J., & Xu, L.-H. 2012a, ApJ, 747, 37

Villanueva, G. L., Magee-Sauer, K., & Mumma, M. J. 2013, JQSRT, 129, 158
Villanueva, G. L., Mumma, M. J., Bonev, B. P., et al. 2012b, JQSRT, 113, 202
Villanueva, G. L., Mumma, M. J., Bonev, B. P., DiSanti, M. A., & Gibb, E. L. 2009, ApJL, 690, L5
Villanueva, G. L., Mumma, M. J., DiSanti, M. A., et al. 2011a, Icar, 216, 227
Villanueva, G. L., Mumma, M. J., DiSanti, M. A., et al. 2012c, Icar, 220, 291
Villanueva, G. L., Mumma, M. J., & Magee-Sauer, K. 2011b, JGRE, 116, 08012
Villanueva, G. L., Mumma, M. J., Novak, R. E., & Hewagama, T. 2008, Icar, 195, 34
Villanueva, G. L., Smith, M. D., Protopapa, S., Faggi, S., & Mandell, A. M. 2018, JQSRT, 217, 86
Wang, Z., Zhang, S.-B., Tseng, W.-L., et al. 2020, AJ, 159, 240
Wooden, D. H., Woodward, C. E., & Harker, D. E. 2004, ApJ, 612, L77
Xie, X., & Mumma, M. J. 1996, ApJ, 464, 457
Zolensky, M. E., Zega, T. J., Yano, H., et al. 2006, Sci, 314, 1735